Materials Advances

Accepted Manuscript

This article can be cited before page numbers have been issued, to do this please use: M. Shoaib Bilal, M. Arslan, S. Javaid, A. Zafar, A. Khalid, S. Karim, N. Ahmad, A. Javed, A. Ghaffar, A. Nisar and M. Ahmad, *Mater. Adv.*, 2026, DOI: 10.1039/D5MA01325A.

View Article Online
DOI: 10.1039/D5MA01325A

PAPER

Unlocking High-Energy and Long-Life Supercapacitors via Zn–MnO_2/MoS_2 Heterostructure Engineering

Received 00th January 20xx,
Accepted 00th January 20xx

DOI: 10.1039/x0xx00000x

Muhammad Shoaib Bilal [a, b], Muhammad Arslan [a, c], Saqib Javed [d], Amina Zafar [e], Atia Khalid [f], Shafqat Karim [a], Naeem Ahmad [g], Athar Javed [h], Abdul Ghaffar [*b], Amjad Nisar [*a] and Mashkoor Ahmad [*a]

Materials engineering plays a pivotal role in determining the energy storage efficiency of supercapacitors. In this work, a Zn–MnO_2/MoS_2 heterostructure was synthesized via a hydrothermal route, where the synergistic coupling of Zn-doped MnO_2 with conductive MoS_2 nanosheets significantly enhanced redox activity, electronic conductivity, surface area and structural stability. Zn doping not only expanded the MnO_2 lattice to facilitate faster ion diffusion but also induced oxygen vacancies, providing additional active sites for charge storage. Meanwhile, MoS_2 offered a conductive 2D framework that buffered volume changes and accelerated electron transport. As a result, the Zn–MnO_2/MoS_2 electrode delivered a high capacitance of 1440 F g^{-1} at 2.85 A g^{-1}, outperforming individual Zn–MnO_2 (1250 F g^{-1}) and MnO_2/MoS_2 (1370 F g^{-1}) as well as previously reported electrodes in 1 M KOH. Furthermore, the assembled Zn–MnO_2/MoS_2//AC device exhibited a specific capacitance of 147 F g^{-1} at 2.85 A g^{-1}, an excellent energy density of 59 Wh kg^{-1} at a power density of 1145 W kg^{-1} and outstanding cycling stability with ~91% retention over 14,000 cycles. These experimental and theoretical insights highlight the strong potential of Zn–MnO_2/MoS_2 heterostructures for next-generation practical supercapacitor applications.

1. Introduction

In the past decade, the extensive use of fossil fuels has resulted serious environmental damage, leading to increased interest in renewable and sustainable energy sources. Among these, electrochemical energy storage systems particularly lithium-ion batteries and supercapacitors (SCs) have become prominent portable and environmentally friendly power sources.[1] However, each system has inherent limitations. For instance, batteries often suffer from gradual material degradation over time and low power density.[2] In contrast, SCs are emerging as promising alternatives particularly for applications such as uninterrupted power supplies, energy storage systems and hybrid vehicles. They offer significant benefits, including exceptionally high theoretical energy density, superior power density, rapid charge–discharge capability and broad operational temperature tolerance.[3] Despite these benefits, SCs face critical challenges most notably their limited practical specific capacitance and cycling stability, which constrain their broader applicability. One of the most important factors influencing the performance of SCs is selection of electrode material.[4] So far, researchers have investigated numerous materials involving various transition metal-based compounds, graphene, conducting polymers, carbon nanotubes and metal-organic frameworks for instance hydroxides, phosphides and sulfides.[5-9] Despite their excellent electrochemical performance, these materials remain impractical for widespread use due to their scarcity and high production costs. In contrast, MnO_2 has garnered considerable attention due to the multivalence of Mn, its low cost, abundance, high theoretical capacitance and environmental friendliness.[10] However, despite its high theoretical capacitance, the practical deployment of pristine MnO_2 is significantly limited by its intrinsically low electrical conductivity. This results in inferior rate capability, sluggish charge-transfer kinetics and restricted utilization of electroactive sites. Consequently, the experimentally observed capacitance rapidly deteriorates at high current densities and remains well below the theoretical value.[11] Therefore, to resolve these issues, various MnO_2-based composites including MnO_2–NiO, MnO_2/ZnO, Mn_2O_3-SnO_2, MnO_2/C, Fe_2O_3/MnO_2/rGO, MnO_2/Graphene/CNT, CNTs@MnO_2@Polypyrrole and Carbon nanosheets/MnO_2/$NiCo_2O_4$ have been examined as electrode materials to mitigate these constraints for SCs applications.[12-19] These materials have improved the surface area and volume expansion of MnO_2-based electrodes. However, the trade-off between electrical conductivity, long-term cycling stability and energy density in the development of practical SCs remains a major bottleneck. These limitations require rational materials engineering to improve the electronic structure and transport pathways of MnO_2.

Doping engineering has proven to be an effective strategy for tailoring the electronic properties and lattice structure of MnO_2. In particular, Zn^{2+} doping enhances electrical conductivity and ion-transport kinetics by introducing defect states, oxygen vacancies and inducing lattice distortion.[20] However, doping alone often provides

[a]Nanomaterials Research Group, Physics Division, PINSTECH, Islamabad 44000, Pakistan.
[b]Department of Physics, Government College University, Lahore 54000, Pakistan.
[c]School of chemical & Material Engineering, NUST, Islamabad, Pakistan
[d]Theoretical Physics Division, PINSTECH, Islamabad 44000, Pakistan
e School of Material science and Engineering, Tsinghua University, Beijing, China.
f Central Analytical Facility Division, PINSTECH, Islamabad 44000, Pakistan
g Faculty of Basic & Applied Sciences, Department of Physics, IIU, Islamabad 44000, Pakistan.
h Department of Physics, University of the Punjab, Lahore, Pakistan.
Correspondence:
Mashkoor Ahmad; mashkoorahmad2003@yahoo.com
Amjad Nisar: chempk@gmail.com
Abdul Ghaffar:abdulghaffar@gcu.edu.pk

limited improvement, as long-range electron transport remains a critical challenge. To mitigate this limitation, constructing heterostructures with conductive frameworks offers a complementary and efficient approach.

Two-dimensional transition-metal dichalcogenides (MoS_2), have attracted significant attention as conductive frameworks owing to their layered structure and favorable electrical properties.[21] Integrating MnO_2 with a 2D MoS_2 framework creates abundant heterointerfaces, shortens ion-diffusion pathways and facilitates rapid electron transport.[22] Moreover, the synergistic coupling between doped MnO_2 and MoS_2 is expected to further improve structural stability during electrochemical cycling. For example, Md. Roxy Islam et al. designed MoS_2/MnO_2 nanocomposite achieved 95% retention after 10,000 cycles with 199 F g^{-1} capacitance at 0.04 A g^{-1}.[23] Jing Ran et al. developed a hollow MnO_2@MoS_2/RGO structure delivering 743 F g^{-1} and sustaining 88.5% capacity over 5,000 cycles.[24]

In the present work, the Zn-MnO_2/MoS_2 heterostructure was successfully synthesized using a hydrothermal technique and assessed for SCs applications. The fabricated Zn-MnO_2/MoS_2 electrode exhibited specific capacitance of 1440 F g^{-1} at 2.85 A g^{-1}. Moreover, the assembled asymmetric coin cell device providing significant energy density of 59 Wh kg^{-1} at a power density of 1145 W kg^{-1}. Additionally, the device retained 91% of its capacity after 14,000 cycles, validating remarkable electrochemical stability and significant potential for next-generation energy storage devices.

2. Experimental section

2.1. Chemicals and Reagents

Manganese chloride tetrahydrate ($MnCl_2{\cdot}4H_2O$), potassium hydroxide (KOH), zinc acetate dihydrate ($Zn(CH_3COO)_2{\cdot}2H_2O$), ethanol and acetone were acquired from Shanghai Aladdin Biochemical Technology Co., Ltd. Potassium permanganate ($KMnO_4$) was procured from Shanghai Macklin Biochemical Co., Ltd. Sodium molybdate dihydrate ($Na_2MoO_4{\cdot}2H_2O$), manganese sulfate monohydrate ($MnSO_4{\cdot}H_2O$) and Thiourea (CH_4N_2S) were supplied by Nanjing Wanking Chemical Glassware and Instrument Co., Ltd.

2.2.Synthesis of Zn-MnO_2/MoS_2

The synthesis of Zn-MnO_2/MoS_2 heterostructure has been carried out as following. In the first step, Zn-MnO_2 nanorods were synthesized according to the previously reported work via hydrothermal method.[25] Initially, 0.5 M manganese chloride tetrahydrate ($MnCl_2{\cdot}4H_2O$) and 0.025 M zinc acetate dihydrate ($Zn(CH_3COO)_2{\cdot}2H_2O$) were dissolved in 50 mL of deionised (DI) water, subsequently undergoing sonication for 30 minutes using probe sonicator. The prepared solution was placed into a 50 ml stainless steel Teflon-lined autoclave and reaction carried out at 140 °C for 12 hours.

Secondly, 0.3 M thiourea (CH_4N_2S) and 0.2 M sodium molybdate (Na_2MoO_4) were prepared in DI water and added to the already prepared Zn–MnO_2 aqueous solution. The mixture was agitated for 1 hour in order to produce a homogenous solution. The final solution was poured in a stainless-steel autoclave lined with Teflon and hydrothermally treated at 200 °C for 24 hours. After natural cooling to room temperature, the resultant brown precipitate was collected by filtering and thoroughly washed with acetone and ethanol. Finally, the product was dried at 70 °C for 5 hours. For comparison, a similar process was adopted to synthesize the pristine MnO_2, MoS_2 and MnO_2 /MoS_2 nanostructures without the addition of Zinc precursors.

2.3. Microstructural Characterization

X-ray diffraction (XRD, Bruker D8 Advance) was utilized to analyse the structural properties of the synthesised materials. High-resolution transmission electron microscopy (HRTEM, JEOL JEM-201, 200 kV, Energy-dispersive spectroscopy (EDS) was implemented along field emission scanning electron microscopy (FE-SEM, TESCAN MIRA-3) and) evaluating the surface morphology and elemental composition. Raman spectroscopy was performed out utilising a Horiba Xplora system excitation laser was used to study vibrational modes of synthesized material. X-ray photoelectron spectroscopy (XPS) was employed to assess the surface chemistry and elemental oxidation states of sample using at the Super ESCA beamline of the ELETTRA synchrotron facility in Trieste, Italy. To get the Brunauer–Emmett–Teller (BET) specific surface area, N_2 adsorption–desorption isotherms were analysed. To further clarify the reaction kinetics, Density functional theory (DFT) calculations were performed.

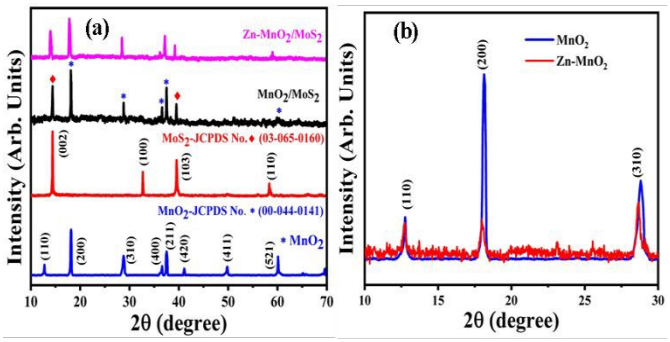

Fig. 1. (a) Typical XRD spectra of MnO_2, MoS_2, MnO_2/MoS_2 and Zn-MnO_2/MoS_2 heterostructure (b) Comparison XRD inset of Zn-doped and pristine MnO_2.

2.4. Electrochemical measurements

Electrochemical measurements of the fabricated MnO_2, MoS_2, Zn-MnO_2, MnO_2/MoS_2 and Zn–MnO_2/MoS_2 electrodes (mass loading ~2 mg cm^{-2}) were performed using a CHI660E electrochemical workstation in 1 M KOH aqueous electrolyte. A three-electrode configuration was employed, with the synthesized MnO_2-based heterostructure as the working electrode, platinum as the counter and Ag/AgCl as the reference electrode. Cyclic voltammetry (CV) was conducted at scan rates of 10–80 mV s^{-1}, galvanostatic charge–discharge (GCD) at current densities in the range of 2.85-11.47 A g^{-1}. The electrochemical impedance spectroscopy (EIS) was performed across the frequency range of 0.1 Hz–140 kHz.

The specific capacitance (C⍰) was determined from the GCD curves using the subsequent equation:

$$C_s=\frac{I*\Delta t}{m*\Delta V} \qquad (1)$$

Where, m represents the active mass of materials, Δt denote the discharge period, I signify the discharge current, and ΔV indicate the voltage window width including IR drop.

2.5 Fabrication of an Asymmetric Supercapacitor (Zn-MnO_2/MoS_2//AC) device

An asymmetric supercapacitor device (Zn–MnO_2/MoS_2//AC) was fabricated using Zn–MnO_2/MoS_2 serving as the positive electrode,

while activated carbon (AC) was employed as the negative electrode. The cell employed a cellulose membrane separator (Whatman GF/D, thickness ~0.2 mm) electrolyte to provide ionic conductivity while avoiding electrode contact and an aqueous solution of 1 M KOH. The electrochemical performance of the assembled device was evaluated using a two-electrode configuration. The active mass of material on the positive (m^+) and negative (m^-) electrodes was calculated based on the charge balance condition ($q^+ = q^-$), expressed by the following relation:

$$\frac{M^+}{M^-}=\frac{Cs^-V^-}{Cs^+V^+} \qquad (2)$$

Moreover, the power (P) and energy (E) density of device were measured by following equation

$$E = \frac{Cs*\Delta V^2}{7.2} \qquad (3)$$

$$P = \frac{(3600*E)}{\Delta T} \qquad (4)$$

2.6 Computational Features

DFT computations have been conducted using the plane-wave pseudopotential scheme of the VASP algorithm.[26] This research employed the Perdew–Burke–Ernzerhof (PBE) functional to model exchange–correlation interactions inside the generalized gradient approximation (GGA) framework.[27] To model the α-MnO_2 phase, a primitive tetragonal unit cell validated by experimental data, using the optimal lattice parameters c = 2.925 Å and a = b = 9.907 Å. One Zn atom was substituted for one Mn atom, resulting in a doping concentration of around 6%. For defect computations, interactions between periodic pictures of defects were minimized using a √2 × √2 × 1 supercell of 48 atoms. The rotationally invariant Hubbard U correction was used to handle electronic correlation effects, yielding effective U values of 3.9 eV for Mn and 4.7 eV for Zn, as adopted from prior computational studies.[28-31] A ferromagnetic spin configuration was applied to α-MnO_2 in alignment with previous theoretical reports.[32] The execution of a 500 eV kinetic energy cutoff resulted in the truncation of the plane-wave basis set. The convergence criteria were established at 0.025 eV/Å for ionic relaxation forces and 1 × 10^{-5} eV for total energy. A 3 × 3 × 12 Monkhorst–Pack k-point mesh was utilized for the primitive cell in order to execute Brillouin zone integrations:

$$E_f(V_0) = E(V_0) - E(bulk) + E(0) \qquad (5)$$

Herein, E (V_0), and E(bulk) are the total energies of the defective and pristine supercells, respectively, and E(O) is the chemical potential of a single oxygen atom. The value of E(O) was taken as -4.52 eV, consistent with high-throughput computational databases.

3. Results and discussion

3.1 Morphological, Structural and compositional analysis

The phase composition and crystalline structure of MnO_2, MoS_2, MnO_2/MoS_2 and Zn-MnO_2/MoS_2 heterostructures was employed using XRD as depicted in Fig. 1(a). The characteristic diffraction peaks identified at 12.71° (110), 18.01° (200), 28.62° (310), 36.49° (400), 37.52° (211), 41.20° (420), 49.63° (411) and 60.13° (521) revealed tetragonal phase (space group, I4/m) of α-MnO_2 as supported by the (JCPDS No. 00-044-0141).[32] The exclusive peaks at 2θ = 14.41°, 32.98°, 38.33° and 58.33°, were precisely correlated with the (002), (100), (103), and (110) diffraction planes of the hexagonal 2H-MoS_2 (molybdenite phase, JCPDS No. 03-065-0160), respectively.[33] Furthermore, the XRD pattern of the MnO_2/MoS_2 composite exhibits characteristic diffraction peaks of both α-MnO_2 (marked with *) and MoS_2 (denoted by □), confirming the successful formation of the MnO_2/MoS_2 heterojunction. Similarly, the Zn–MnO_2/MoS_2 heterostructure retains the prominent diffraction peaks of α-MnO_2 including the (200), (310), (400), (211), and (521) planes, together with the characteristic peaks of MoS_2. No additional impurity peaks are detected, verifying the effective synthesis of Zn-MnO_2/MoS_2 heterostructure without the formation of secondary phases. The inset of Fig. 1(b) presents a comparison of Zn-doped and pristine MnO_2 in the 2θ range of 10–30º corresponding to (110), (200) and (310) peaks. A careful examination reveals a slight shift of these diffraction peaks toward lower angles upon Zn doping. This peak shift can be attributed to lattice expansion induced by charge imbalance and lattice distortion arising from the incorporation of Zn^{2+} ions into the MnO_2 crystal lattice. Such lattice distortion is indicative of successful Zn doping and may generate local strain and defect sites, which are expected to influence the structural and electrochemical properties of the material.[34]

The structural vibration modes of molecules of Zn–MnO_2/MoS_2 heterostructure were examined by employing Raman spectroscopy. Fig. 2 presents the Raman spectra of MnO_2, Zn–MnO_2, MoS_2 and Zn–MnO_2/MoS_2 heterostructure. As observed, the spectra exhibit modes at 382, 405 and 635 cm^{-1}. The distinctive peak at 635 cm^{-1} correlate to the A_1g mode of MnO_2, arising from the breathing vibrations of [MnO_6] octahedral.[35] The prominent peaks noted at 405 and 382 cm^{-1} attributed to the A_1g and E^1_2 g phonon modes of 2H-MoS_2, respectively.[36] Moreover, the presence of characteristic

Fig. 2. Raman shift of MnO_2, MoS_2, Zn-MnO_2, and Zn-MnO_2/MoS_2

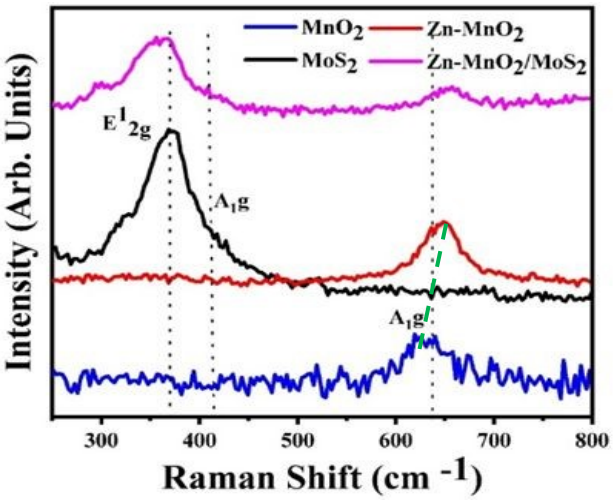

heterostructure

vibrational modes of both MnO_2 and MoS_2, to verify the successful formation of the heterostructure. Additionally, Zn doped MnO_2 shows a shift towards higher wavenumbers as clearly indicated by green dotted line, and consistent with previously reported studies.[37] This shift can be attributed to changes in the local bonding environment and lattice strain caused by Zn incorporation, as well as interactions at the MoS_2 interface.

Fig. 3(a-c). presents the N_2 adsorption–desorption isotherms and pore size distribution of MnO_2, MoS_2, and the Zn–MnO_2/MoS_2

heterostructure measured at 77 K. All samples exhibited Type IV adsorption–desorption isotherms with H_3-type hysteresis loops, confirming the predominance of mesoporous channels. Notably, the Zn–MnO_2/MoS_2 heterostructure shows a markedly higher adsorption volume across the entire relative pressure (p/p_o) range compared with pristine MnO_2 and MoS_2. The specific surface area of the heterostructure is calculated to be 215 m^2/g, substantially exceeding that of MnO_2 (85 m^2/g) and MoS_2 (45 m^2/g). Morever, Fig. 3(b) and 3(c) present the BJH pore size distribution curves derived from the N_2 desorption isotherms. The Zn-MnO_2/MoS_2 composite exhibits a relatively uniform mesoporous structure, with a narrow pore size distribution centered in a narrow pore size distribution predominantly located within the mesoporous region (≈3–10 nm). In contrast, pristine MnO_2 and MoS_2 display broader pore size distributions extending towards larger mesopores, indicating a higher degree of structural heterogeneity. The pronounced peak observed in the pore size distribution confirms the formation of well-defined mesopores, which is advantageous for electrochemical energy storage applications. Moreover, the combination of high surface area and accessible mesopores facilitates enhanced electrode–electrolyte contact, thereby improving ion transport kinetics and charge storage efficiency.This enhancement is can be ascribed to the synergistic effects of MoS_2 integration and Zn doping, which presumably create structural defects and promote the formation of additional accessible mesopores. The mesopores enhance rapid ion transport consequently augmenting the material's power output and rate capability.[38] Such an engineered architecture facilitate abundan active sites, thereby fulfilling the structural requirements for high-performance energy storage devices .[39-41]

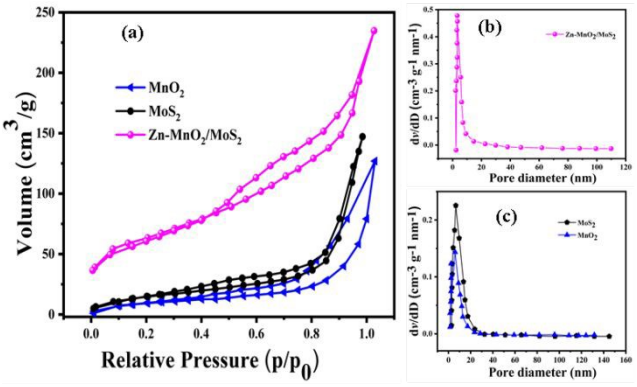

Fig. 3. (a) N absorption-desorption isotherm (b) distribution of pore size behaviour of Zn-MnO_2/MoS_2 and (c) pore size behaviour of both MnO_2 and MoS_2

Fig. 4(a) displays the morphology of the MnO_2 which consists of high-quality nanorods with length in microns and uniform diameter in the range of nanometers. Fig. 4(b) presents the surface morphology of the MoS_2 structure. The microstructure consists of loosely packed, sheet-like structure composed of thin, layered nanosheets with irregular edges. These nanosheets are interconnected, forming a porous, flower-like architecture with abundant voids and interlayer spacing. Fig. 4(c) displays the morphology of Zn-MnO_2/MoS_2 heterostructure. The developed material is composed of irregularly shaped, agglomerated nanosheets with a rough texture, along with distinct, rod-like or needle-shaped nanostructures distributed throughout the matrix. The composite structure clearly shows the successful integration of MoS_2 nanosheets with Zn-doped MnO_2 nanorods. The presence of 1D Zn-doped MnO_2 naorods is very suitable for electrochemical energy storage owing to greater surface accessibility and rapid ion diffusion.

The detailed morphological and structural characteristics were analyzed using TEM. Fig. 4(d) emphasizes low-magnification TEM image of pristine MnO_2 indicating randomly dispersed nanorods. These nanorods exhibit a uniform diameter of approximately 75 nm and extend to micrometre-scale lengths. Fig. 4(e) describes the TEM image of MoS_2, revealing well-dispersed and directionally aligned nanosheets. In Fig. 4(f), the Zn-MnO_2/MoS_2 heterostructure displays MnO_2 nanorods anchored onto MoS_2 nanosheets, signifying the successful formation of a hybrid heterostructure. HRTEM as shown in Fig. 4(g), validates the polycrystalline nature of the Zn-MnO_2/MoS_2 composite. Fig. 4(h), extracted from the rectangular region marked in Fig. 2(g), shows clear lattice fringes with measured d-spacing of ~0.31 nm and ~0.27 nm, which corresponds to the (110) plane of MnO_2 and the (100) plane of layered hexagonal MoS_2, respectively. Furthermore, EDS spectrum in Fig. 4(i) reveals prominent peaks for Mo, Mn, S, O and Zn, thereby confirming the successful formation of the composite. In comparison, Fig. S1(a) and S1(b) present EDS spectra of pristine MnO_2 and MoS_2, where the elemental compositions closely match their respective theoretical stoichiometry.

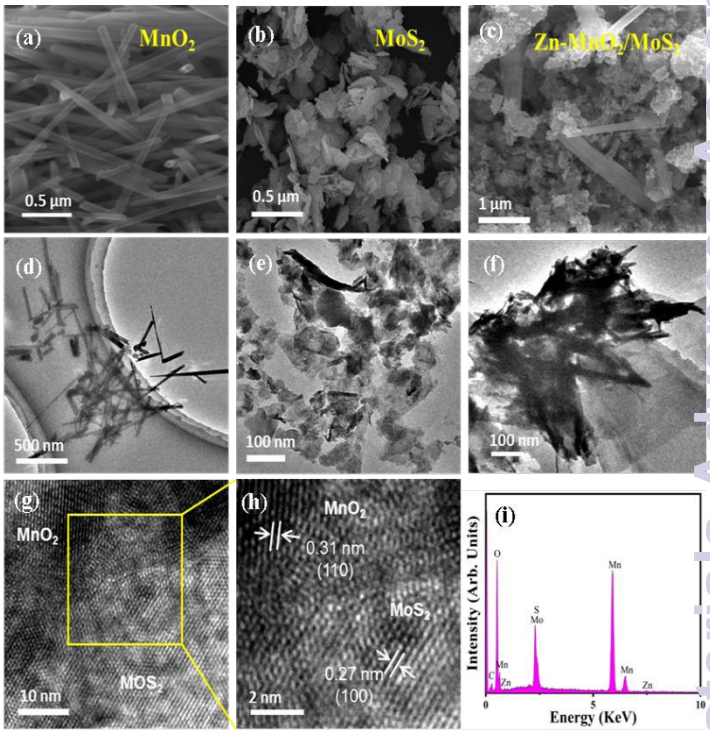

Fig. 4 (a-c) SEM images of Zn-MnO_2/MoS_2 heterostructure network at different magnification (d-f) TEM images (g,h) HRTEM images of Zn-MnO_2/MoS_2 heterostructure (i) EDS spectrum of Zn-MnO_2/MoS_2 hetrerostructure.

XPS analysis was employed to examine the surface valence states of the Zn–MnO_2/MoS_2 heterostructures. Fig. 5(a) presents the XPS spectra of the Mn 2p region. The coexistence of Mn^{3+} and Mn^{4+} state is evidenced by the observation of two distinct peaks in the Mn $2p_3/_2$

region at 644.1 eV (Mn^{4+}) and 642.6 eV (Mn^{3+}). Similarly, the peaks at 655.5 eV (Mn^{4+}) and 653.9 eV (Mn^{3+}) in the Mn $2p_{1/2}$ region further validate the existence of both oxidation states.[42, 43] The energy separation between Mn $2p_{3/2}$ and Mn $2p_{1/2}$ is ~11.86 eV, consistent with the characteristic spin–orbit splitting of Mn in mixed oxidation states.[41] It is noteworthy that oxygen vacancies can induce the formation of trivalent Mn^{3+} indicates the reduction of M^{4+} to M^{3+} by accelerating the kinetics of surface redox reactions.[44] The Mn 2p XPS spectra were analyzed using quantitative peak deconvolution to evaluate the Mn^{3+}/Mn^{4+} ratio. The Mn^{3+}/Mn^{4+} ratio increased from 1.4 (MnO_2) to 3.1 (Zn–MnO_2/MoS_2 heterostructure), indicating an enhanced proportion of Mn^{3+} species upon Zn doping. This increase suggests a higher concentration of oxygen vacancies in the Zn-doped sample. The observed shift in Mn valence states can be attributed to charge compensation effects associated with Zn incorporation, which modifies the local electronic structure and promotes the formation of Mn^{3+} species.[45] Fig. 5(b) presents the spectra of Zn 2p, thereby corroborating the successful incorporation of Zn into host MnO_2. The appearance of two separate peaks at 1023.5 eV and 1046.6 eV relating to Zn^{2+} $2p_{3/2}$ and Zn^{2+} $2p_{1/2}$ states respectively, with a spin–orbit energy of 23.1 eV[46]. Fig. 5(c,d) displays the O 1s spectra emphasizing two prominent peaks at 529.4 eV and 530.7 eV, representing to lattice oxygen (O_{latt}) and surface oxygen vacancies (O_v) respectively[47]. Significantly, the enhanced oxygen vacancies in heterostructure are evidenced by the increase in intensity ratio (O_v/O_{latt}) ~ 0.56 than pristine MnO_2 (0.44). As seen inFig. 3(e), the Mo 3d spectrum was deconvoluted into two discrete peaks located at 228.2 eV and 231.6 eV corresponding to Mo^{4+} $3d_{5/2}$ and $3d_{3/2}$ respectively. Fig. 5(f) illustrates the S 2p spectra, which exhibits discrete peaks at 161.1 eV and 162.3 eV associated with S^{2-} $2p_{3/2}$ and S^{2-} $2p_{1/2}$ of MoS_2, respectively. All of these XPS findings support the effective synthesis of the Zn-MnO_2/MoS_2 heterostructure and are in good agreement with the literature.[48-50]

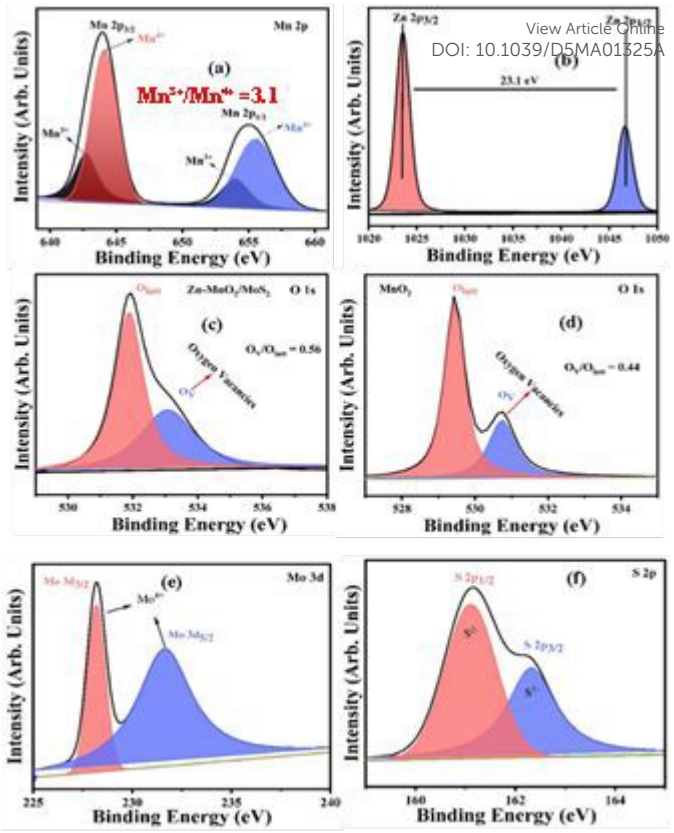

Fig. 5. XPS analysis of Zn-MnO_2/MoS_2, high resolution spectrum of (a) Mn 2p (b) Zn 2p (c,d) O 1s (e) Mo 3d (f) S $^{-2}$

3.2 Electrochemical measurements

3.2.1 Cyclic Voltammetry

Fig. 6(a) reveals the comparative CV profiles of MnO_2, MoS_2, Zn–MnO_2, MnO_2/MoS_2 and Zn–MnO_2/MoS_2 electrodes measured at a scan rate of 10 mV s^{-1} within stable potential window of -0.4 to 0.6 V. All electrodes show approximately rectangular CV curve and demonstrate pseudo-capacitance behaviour. In comparison, the area under the CV curve of the Zn–MnO_2/MoS_2 electrode is higher than its individual counterparts (Zn-MnO_2 and MnO_2/MoS_2) electrodes. The significantly enhanced enclosed area of the curve is considered due to the increase in active sites and surface area. Fig. 6(b) depicts the CV response of Zn–MnO_2/MoS_2 electrode at different sweep rates in the range ~10 to 80 mV s^{-1}. It is found that, the enclosed area of the CV loop correspondingly increases with the increase in scan rate, reflecting an increase in capacitive current. The shape of the CV curves remains constant across various scan rates indicating excellent electrochemical reversibility and symmetrical redox kinetics. However, it is found that, at higher scan rates, slight distortions in loop closure are observed, likely due to kinetic limitations associated with multi-electron redox transitions Mn^{4+}/Mn^{3+} and Mo^{4+}/Mo^{3+}. These processes demand sufficient time for ion migration and interfacial charge redistribution, which becomes rate-limiting under rapid scanning conditions.[38] In comparison, the CV responses of MnO_2, MoS_2, Zn–MnO_2 and MnO_2/MoS_2 electrodes at various sweep rates are presented in Fig. S3(a-d). Fig. 6(c) elucidates the relation between scan rate (v) and peak current (i) obtained from the CV curves shown in Fig. 6(b) offering valuable insights into its underlying charge storage mechanism. The relationship between the scan rate and peak current is described by power law.

$$i = av^b \qquad (6)$$

Typically, the b-value is found using the log(i) against log (v) plot, in which b is the slope of the linear fit. A b-value close to 0.5 and 1.0 corresponds to diffusion and surface-driven capacitive controlled mechanisms, respectively, thereby highlighting the dominant kinetic process governing the electrode behaviour.[51, 52] The computed b-values from Fig. 6(c), 0.65 and 0.67, confirm the coexistence of both diffusions controlled and capacitive charge storage mechanisms in the Zn–MnO_2/MoS_2 electrode. Additionally, based on the CV curves, the reaction kinetics were further investigated using Dunn's equations to distinguish between capacitive and diffusion-controlled contributions.[53]

$$i(v) = K_1 v + K_2^{(1/2)} \qquad (7)$$

The equation has been modified to,

$$\frac{i(v)}{v^{(1/2)}} = K_1 v^{(1/2)} + K_2 \qquad (8)$$

Here, i and v stand for current and scan rate, respectively, and k_1v and $k_1v^{(1/2)}$ for capacitive and diffusion currents, respectively. Fig. 6(d) reveals the charge contribution of the Zn–MnO_2/MoS_2 electrode at different sweep rates. At a low sweep rate of 10 mV s^{-1}, a significant portion of the charge arises from diffusion-controlled processes, as ions possess enough time to permeate into the bulk of the electrode and participate in faradaic redox reactions, while the capacitive contribution accounts for nearly 75%. With increasing scan rate (20–40 mV s^{-1}), the capacitive contribution progressively dominates, since the reduced diffusion time limits ion insertion into inner active sites, thereby favouring surface-controlled storage. At higher scan rates (60–80 mV s^{-1}), the capacitive mechanism overwhelmingly prevails, contributing over 90% of the total charge. Even at high scan rate, the composite's extensive mesopores allow for efficient charge storage by reducing ion diffusion pathways and accelerating electrolyte penetration. A wide interfacial area and continuous electron transport channels are also provided by the 2D conductive MoS_2 framework, which greatly enhances the surface-controlled capacitive process. Zn-MnO_2 and MoS_2 have a strong covalent interfacial contact that facilitates rapid redox reactions and lowers charge transfer resistance. This trend demonstrates that the electrode exhibits a rapid charge storage response, with capacitive behaviour dominating at fast sweep rates, underscoring its potential and excellent rate capability for high-power energy storage applications.

3.2.2. Galvanostatic charge-discharge (GCD)

Fig. 6(e) represents the comparative GCD profiles of MnO_2, MoS_2, Zn–MnO_2, MnO_2/MoS_2 and Zn–MnO_2/MoS_2 electrodes, measured within a stable potential window of –0.2 to 0.6 V at a current density of 2.85 A g^{-1}. The nearly symmetrical triangular shaped GCD curves confirms the characteristic capacitive behavior exhibited by all electrodes. Notably, the Zn–MnO_2/MoS_2 heterostructure electrode exhibits a prolonged discharge time relative to the other three electrodes, suggesting enhanced charge storage capability. Fig. 6(f) reveals the GCD curves of the Zn–MnO_2/MoS_2 electrode at different current densities ranging from 2.85 to 11.43 A g^{-1}. The specific capacitance of the electrodes was determined from the GCD measurements based on equation (1), The calculated specific capacitance values at 2.85, 5.71, 8.57 and 11.43 A g^{-1} are 1440, 1184, 980 and 870 F g^{-1}, respectively. The electrode achieved a maximum specific capacitance of 1440 F g^{-1}at a current density of 2.85 A g^{-1}. At higher current density 11.43 A g^{-1} the electrode maintains specific capacitance of 870 F g^{-1} with a retention of around 60%, showing outstanding rate capability. For comparison, the GCD curves of the MnO_2, MoS_2, Zn-MnO_2 and MnO_2/MoS_2 electrodes are also measured at different current densities as represented in Fig. S4(a-d). Furthermore, the specific capacitance values of all five electrodes across the same current density range (2.85 to 11.43 A g^{-1}) are demonstrated in Fig. 6(g). These findings provide clear evidence that the heterostructure electrode offers improved capacitance. The heterostructure electrode achieved much better capacitance than the pristine MnO_2, MoS_2, Zn-MnO_2 and MnO_2/MoS_2 as well as previously reported MnO_2 based electrodes as shown in Table 1.

3.2.3. Electrochemical impedance spectroscopy (EIS)

EIS performed to explain the charge transfer, ion diffusion mechanism and kinetics of electron within electrodes materials in 1M KOH electrolyte. Fig. 6(h) presents the Nyquist plots illustrating the imaginary and real components of impedance for the MnO_2, MoS_2, Zn–MnO_2, and Zn–MnO_2/MoS_2 electrodes. The Nyquist plots exhibit semicircular and linear slopes in the high-frequency region. The semicircle diameter at the electrode–electrolyte interface is directly related to the charge transfer resistance (R_{ct}). The semi-circle of the bare MnO_2 electrode is greater than MoS_2, Zn-MnO_2 and Zn-MnO_2/MoS_2 electrodes. In contrast, the Zn–MnO_2/MoS_2 heterostructure exhibits the smallest semicircle diameter, demonstrating the lowest R_{ct} among all samples. An AC equivalent circuit model as illustrated in Fig. 4(h) reveals that the measured R_{ct} value for the MnO_2, MoS_2, Zn–MnO_2, MnO_2/MoS_2 and Zn–MnO_2/MoS_2 electrodes are 204, 128.9, 78.56, 65.03 and 44.07 Ω, respectively. The fitting parameters of synthesized electrodes are shown in Table 2. The notably low R_{ct} value of the Zn–MnO_2/MoS_2 electrode indicates the high intrinsic conductivity of MoS_2 and the generation of oxygen vacancies induced by Zn reflects excellent electrical conductivity within the electrochemical system. The synergistic interaction between Zn–MnO_2 and MoS_2 significantly improved reaction kinetics, resulting in exceptional electrochemical energy storage capability.

Fig. S6 presents the Bode phase plots for MnO_2, MoS_2, Zn–MnO_2, MnO_2/MoS_2, and Zn–MnO_2/MoS_2 heterostructures, elucidating the frequency-dependent electrochemical kinetics. A 0° phase angle signifies a perfect resistor, +90° indicates an ideal inductor, and -90° denotes an ideal capacitor. At high frequencies, it is crucial to observe that the phase angle decreased for all electrodes owing to the increasing effects of ohmic resistance and diffusion constraints. That being said, Zn–MnO_2/MoS_2 retains a relatively greater phase angle, which is indicative of lower internal resistance and more effective electron–ion transport. In the middle frequency range (10^2–10^3 Hz), the phase angle attains a maximum that corresponds to the characteristic relaxation frequency related to interfacial charge transfer. The Zn–MnO_2/MoS_2 electrode exhibits this peak at a higher frequency and a less negative phase angle compared to the other samples, signifying accelerated charge-transfer kinetics and a reduced time constant, attributable to the synergistic interaction between Zn-doped MnO_2 and conductive MoS_2. At low frequency ranges (10–10^2 Hz), all electrodes display significant negative phase angles, signifying the prevalence of capacitive and pseudocapacitive processes resulting from surface redox reactions and ion adsorption. The Zn–MnO_2/MoS_2 electrode exhibited a smaller negative phase angle, indicating a more optimal capacitive response, contributed to better electrolyte accessibility and an increase in electroactive sites within the hybrid structure. This reaction highlights limitations in mass transport, such as the diffusion of ions through the electrolyte or within a porous electrode structure.

3.3 DFT Calculations

DFT calculations were employed to support and validate the main experimental results, with an emphasis on the contribution of Zn doping in α-MnO_2 played in improving the electrode's electrochemical performance. Fig. 7(a,b) presents the partial density of states (PDOS) for both α-MnO_2 and Zn-MnO_2. For MnO_2, a noticeable band gap of approximately 1.0 eV is observed, indicative of its semiconducting nature. Upon Zn incorporation, the band gap closes, leading to a metallic ground state. This transition implies a significant enhancement in the electronic conductivity of MnO_2 due

to Zn doping, predicted to enhance the kinetics of the redox process at the electrode. In addition to electronic structure, the impact of Zn doping on defect formation was also investigated by calculating the oxygen vacancy formation energy for a nearest-neighbor O atom. The vacancy formation energy for MnO_2 is found to be 1.55 eV, whereas for the O atom adjacent to the Zn dopant, the energy decreases significantly to 0.30 eV. This substantial reduction indicates that Zn doping promotes the formation of oxygen vacancies. The close observation shows that oxygen vacancies increase the electrode material specific capacitance by introducing more electrochemically active sites. Furthermore, the formation of a heterostructure between Zn-MnO_2 and MoS_2 is expected to introduce even more active sites benefiting not only from the high surface-to-volume ratio of MoS_2 but also from defect generation during heterostructure formation. Overall, these theoretical insights confirm that Zn doping in MnO_2 enhances both conductivity and defect-induced activity, thereby improving redox kinetics and capacitance. To further corroborate experimental findings, we performed Bader charge analysis to estimate net atomic charges on Mn in MnO2, calculated as difference between electronic population of pristine Mn and that in α-MnO_2. Overall, a net charge of ~ +1.80 e is found on Mn atom in α-MnO_2, suggesting a net electron transfer of ~1.80 e to oxygen atoms, which is good agreement with previous DFT calculations [54]. Interestingly, there is no significant change in Mn Bader charges due to Zn doping. In contrast, a noticeable increase in electronic population is observed due to a single oxygen vacancy such that number of electrons increase by ~ 0.25 e for Mn atom adjacent to oxygen vacancy. Since, Zn dopant promotes oxygen vacancy formation process, this means that the oxidation state of Mn will reduce due to Zn doping, which is qualitatively consistent with experimental results where an increase in Mn3+ population was observed due to oxygen vacancies. These findings are in strong agreement with the experimental observations, validating the synergistic role of Zn doping and heterostructure engineering in optimizing electrochemical performance. Finally, we point out that the study of MnO_2/MoS_2 heterostructure is currently not feasible owing to the two materials having different symmetries, thus requiring a prohibitively large supercell. We nevertheless discuss the possible beneficial effects of such heterostructures.

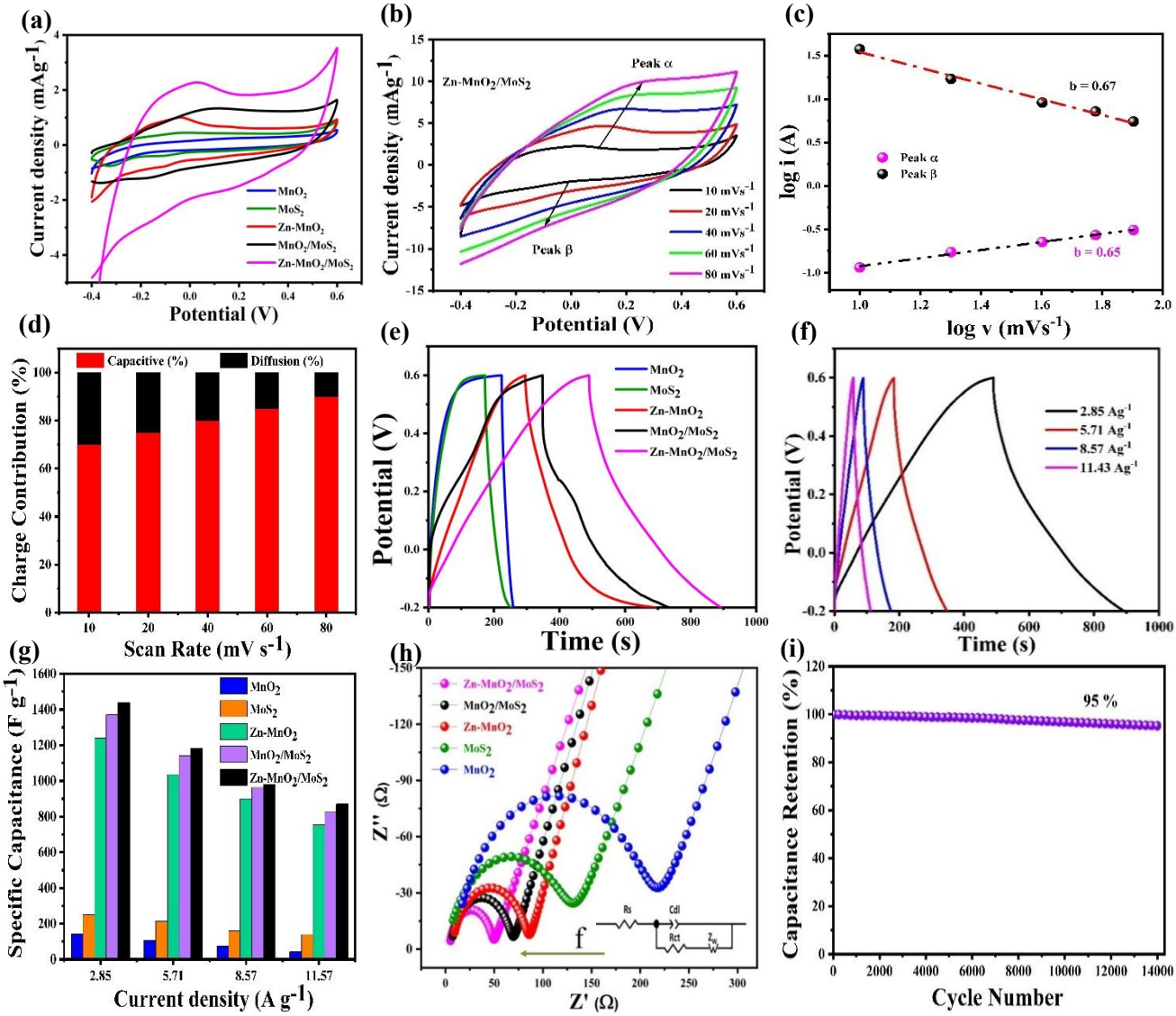

View Article Online
DOI: 10.1039/D5MA01225A

Fig. 6. (a) Comparative CV response at sweep rate 10 mV s^{-1} of all electrodes (b) CV curves of Zn-MnO_2/MoS_2 electrode at different sweep rate (c) Relationship between Log i(A) and Log V(mV s^{-1}) (d) diffusion and capacitive contributions ratios (e) comparative analysis of GCD curve of electrodes at 2.85 A g^{-1} (f) GCD curves of Zn-MnO_2/MoS_2 electrode at kinds of current density (g) the specific capacitance variation of all electrodes (h) Nyquist plot of MnO_2, MoS_2, Zn-MnO_2, MnO_2/MoS_2 and Zn-MnO_2/MoS_2 electrodes; the inset shows the kinetic parameters of electrodes (i) cyclic performance of the Zn-MnO_2/MoS_2 for 14000 cycles at 2.85 A g^{-1}.

3.4 Performance of the Asymmetric supercapacitor (Zn-MnO_2/MoS_2//AC) device

To assess the practical applicability of the synthesized heterostructure, an asymmetric coin cell supercapacitor (Zn–MnO_2/MoS_2//AC) was assembled with activated carbon (AC) as anode and Zn–MnO_2/MoS_2 as the cathode utilizing 1 M KOH/PVA as the electrolyte. Fig. 8(a) highlights the schematic of the fabricated Zn–MnO_2/MoS_2//AC device. It can be shown in Fig. 8(b), the CV curves exhibit a quasi-rectangular shape at scan rates 10 to 60 mV s^{-1}, indicating efficient ion transport and optimal capacitive behavior. As represented in Fig. 8(c), the GCD curves showed approximately symmetrical triangular shapes at current densities ranging from 2.85 to 14.29 A g^{-1}, indicating higher columbic efficiency and superior reversibility. The specific capacitance computed from the GCD data are exhibited in Fig. 8(d). The device possesses outstanding rate capability, offering a high specific capacitance of 147 F g^{-1} at a current density of 2.85 A g^{-1} and retaining 91 F g^{-1} even at 14.29 A g^{-1}. Fig. S7 (a) illustrates the energy density and power density of the device, as calculated using Equations (3) and (4). Remarkably, with a power density of 1145 W kg^{-1}, the device attained an exceptional energy density of around 59 Wh kg^{-1} within a potential window of 0.0–1.7 V, surpassing previously reported MnO_2-based devices.[38, 55-61] Fig. (e) presents radar plot comparing the energy density, power density, operating potential window and specific capacitance achieved in this work with those reported in previous studies, with detailed comparative data provided in Table S2. Fig. 8(f) manifests the Nyquist plot, demonstrating low internal resistance and enhanced charge-transfer kinetics, which signify the device's effective electrochemical performance. As shown in Fig. S7 (b) the cycling stability demonstrates 91% capacitance retention over 14,000 cycles, confirming the superior long-term electrochemical stability of the Zn–MnO_2/MoS_2//AC device. Additionally, the self-discharge behaviour of Zn–MnO_2/MoS_2//AC device demonstrated an extensive voltage drop during the initial phase, with the voltage diminishing from 2.4 volts to around 1.2 volts within the first 10 hours as shown in Fig. S7 (c). Subsequently, the voltage stabilized at approximately 1.0 volts, preserving around 42% of its initial value after 140 hours. Moreover, the average self-discharge rate of the device was approximately 0.42% per hour during 140 hours, however this rate markedly dropped to around 0.05% per hour during the constant voltage phase. In addition, the areal capacitance of the device, shown in Fig. S9, was calculated from the linear GCD curves (Fig. S8). The device exhibits a high areal capacitance of 205 mF cm^{-2} at a current density of 0.5 mA cm^{-2}, demonstrating excellent capacitive performance. This value is comparable to those of recently reported devices listed in Table S1. The improved performance can be ascribed to several synergistic effects: (i) the heterostructure introduce structural defects and abundant electroactive interfaces; (ii) the nanorod–nanosheet morphology promotes rapid ion diffusion and mass transport (iii) Zn doping generates oxygen vacancies, enhancing electrical conductivity and reaction kinetics.

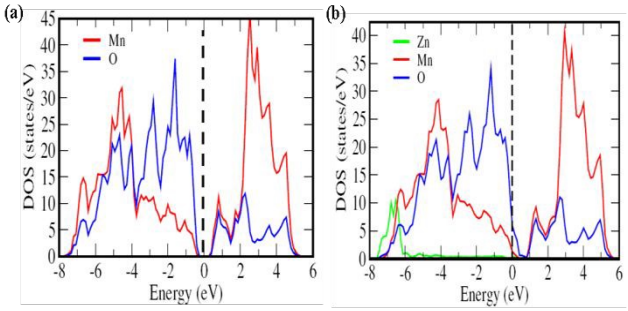

Fig.7 Partial density of states of (a) α-MnO_2 and (b) Zn doped α-MnO_2. The dashed vertical line represents Fermi level.

Conclusion

The Zn–MnO_2/MoS_2 heterostructure was successfully synthesized through a hydrothermal strategy. The combined experimental and DFT analyses confirmed that Zn doping introduces oxygen vacancies and enhances electronic conductivity, leading to superior charge storage capability. Unlike pristine or binary electrodes, the Zn–MnO_2/MoS_2 heterostructure uniquely integrates the high redox activity of MnO_2 with the layered conductivity of MoS_2, while Zn incorporation introduces defect sites that accelerate charge transport, thereby achieving an exceptional specific capacitance of 1440 F g^{-1} at 2.85 A g^{-1}. The asymmetric coin cell (Zn–MnO_2/MoS2//AC) further demonstrated a high energy density of 59 Wh kg^{-1} at 1145 W kg^{-1} with excellent cycling stability (91% retention after 14,000 cycles), underscoring its robustness for long-term operation. The improved performance is the result of synergistic effect of Zn doping and the heterostructure interface, which is rarely achieved in conventional electrode designs. Looking ahead, scalable synthesis, device integration, and hybridization with other 2D systems could advance the Zn–MnO_2/MoS_2 heterostructure toward next-generation supercapacitors for portable electronics, electric vehicles and grid storage.

Author Contributions

M. S. B. performed the experimental work, and was primarily responsible for data collection, analysis, and drafting of the manuscript. M. A. assisted with methodology development, formal analysis, and preparation of figures. S. J. performed the DFT study. S. K. provided supervision and technical resources throughout the study. N. A. contributed to experimental investigations and data curation. A. G. contributed to project administration and supervision. A. N. provided guidance, supervision, and critical revisions of the manuscript. M. A. conceived the overall research idea, supervised the project, and contributed significantly to manuscript writing, review, and editing.

Conflicts of interest

No financial conflicts of interest are declared by the authors.

Acknowledgements

This work was supported by Pakistan Atomic Energy Commission (PAEC). The authors are thankful to COMSTECH, Pakistan and SESAME, Jordan for supporting to perform the experiment at MS beamline under the SESAME users' program. Help and support from ICTP to perform experiment at Elettra – Synchrotron under the ICTP-Elettra users program is also acknowledged.

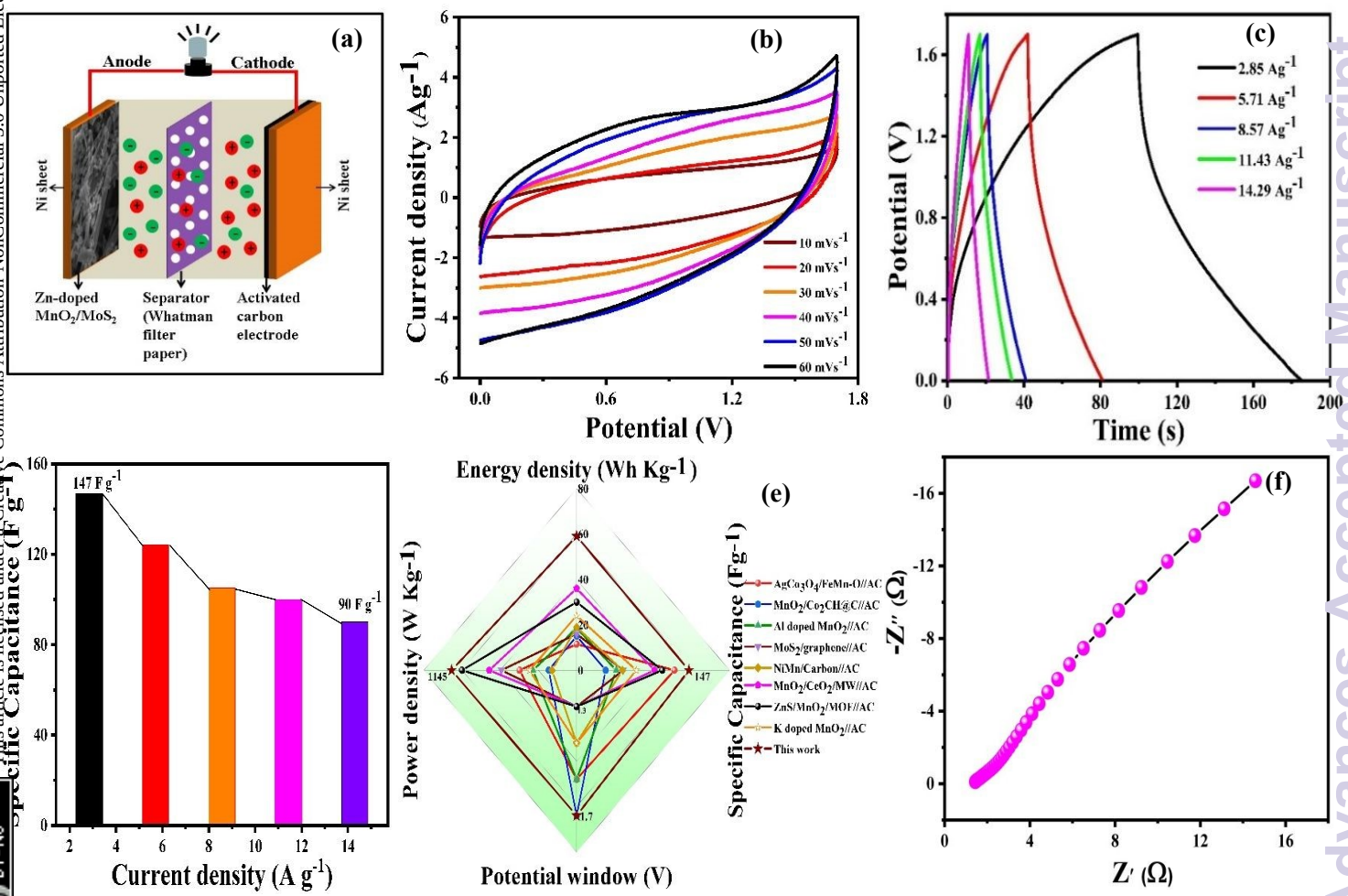

Fig. 8. The electrochemical performance of Zn-MnO_2/MoS_2//AC device (a) Structural illustration of fabricated device (b) CV response at different scanning rates between 10 and 60 mV s^{-1} (c) GCD curves at current density of 2.85 to 11.47 A g^{-1} (d) variation of capacitance at different current densities (e) radar graphs of operating potential window, specific capacitance, energy density and power density of different devices (f) Nyquist plot of Zn-MnO_2/MoS_2//AC.

View Article Online
DOI: 10.1039/D5MA01325A

Table 1 Performance comparison of designed Zn-MnO_2/MoS_2 electrode with previously reported MnO_2-based electrodes.

Material	Electrolyte	Current density (A g^{-1})	Specific capacitance (F g^{-1})	Cycling stability (%)	Charge Transfer Resistance (Rct)	Cycle Number	Ref.
MoS_2/MnO_2	Na_2SO_4	0.04	199.12	95	2.5	10,000	23
MoS_2/Mn_3O_4	Na_2SO_4	1	172	69.3	1.41	2000	62
MoS_2/MnO_2	PVA/H_3PO_4	0.8	212	84.1	700	5000	63
MnO_2@MoS_2	KOH	1	352	72	2	2000	39
POAP/MoS_2/MnO_2	$HClO_4$	1	529	93	2.85	4000	64
$ZnMnO_2$/CC	Na_2SO_4	1	667	92	105.4	8000	31
ZnMnO/HPC	KOH	0.5	400	99.5	15	10,000	65
MnO_2/graphene/PANI	Na_2SO_4	1	870	93	-	5000	66
ZnS/MnO_2	KOH	1	1002	95	0.48	5,000	67
CQDs/ε-MnO_2	Na_2SO_4	1	334	90	3	6,000	68
MnO_2@Co_2NiO_4	KOH	1	1025	73	0.356	5000	69
$MnO_{2-x}F_y$	Mg $(NO_3)_2$	0.5	491.5	84	0.71	10000	70
Zn-MnO_2/MoS_2	**KOH**	**2.85**	**1440**	**95**	**44.07**	**14000**	**This wor'**

Table 2. The fitted parameters of all electrodes

Material	R_s (Ω)	R_{ct} (Ω)
MnO_2	8.05	204
MoS_2	1.19	128.9
Zn-MnO_2	6.65	78.56
MnO_2/MoS_2	5.38	65.03
Zn-MnO_2/MoS_2	**4.42**	**44.07**

References

1. H. Shen, X. Kong, P. Zhang, X. Song, H. Wang and Y. Zhang, Journal of Alloys and Compounds, 2021, 853, 157357.
2. N. S. Padalkar, J. A. Shingade and J. P. Park, Materials Today Physics, 2025, 53, 101711.
3. X. Ren, H. Wang, J. Chen, W. Xu, Q. He, H. Wang, F. Zhan, S. Chen and L. Chen, Small, 2023, 19, 2204121.
4. N. Zahra, M. Shahbaz, M. Saleem, M. Z. Khan, M. Irshad, S. Sharif, J. H. Koh, M. A. Marwat, G. Lee and M. Irfan, Materials Today Sustainability, 2025, 30, 101099.
5. N. Guo, R. Ma, P. Feng, D. Wang, B. Zhang, L. Wang, D. Jia and M. Li, International Journal of Biological Macromolecules, 2024, 262, 130254.
6. R. Liang, Y. Du, P. Xiao, J. Cheng, S. Yuan, Y. Chen, J. Yuan and J. Chen, Nanomaterials, 2021, 11, 1248.
7. R. Fatima, S. Naseer, M. R. H. S. Gilani, M. Aamir and J. Akhtar, Sustainable Materials for Electrochemical Capacitors, 2023, 33-64.
8. C. M. Han and K. S. Lee, Applied Chemistry for Engineering, 2025, 36, 253-259.
9. Z. Huang, W. Zhou, D. Li and J. Xu, The Chemical Record, 2025, 25, e202400233.
10. M. Nepal, G. S. Gudavalli and T. P. Dhakal, ACS omega, 2025, 10, 3439-3448.
11. X. Cao, X. Liu, Q. Zou and W. Sun, RSC advances, 2025, 15, 45480-45499.
12. V. Vinisha, S. Narayanasamy, A. Matharasi, G. Jaffrin and J. M. Linet, Electrochimica Acta, 2025, 518, 145785.
13. B. L. Vijayan, S. G. Krishnan, N. K. M. Zain, M. Harilal, A. Yar, I. I. Misnon, J. O. Dennis, M. M. Yusoff and R. Jose, Chemical Engineering Journal, 2017, 327, 962-972.
14. A. Sayah, N. Boumaza, F. Habelhames, A. Bahloul, H. Bencherif, A. Tounsi, L. Lamiri and B. Nessark, Journal of Materials Science: Materials in Electronics, 2024, 35, 62.
15. J. Jablonskiene, D. Simkunaite, J. Vaiciuniene, G. Stalnionis, A. Drabavicius, V. Jasulaitiene, V. Pakstas, L. Tamasauskaite-Tamasiunaite and E. Norkus, Crystals, 2021, 11, 784.
16. M. Geerthana, S. Prabhu and R. Ramesh, Journal of Energy Storage, 2022, 47, 103529.
17. Y. Liu, D. He, J. Duan, Y. Wang and S. Li, Materials Chemistry and Physics, 2014, 147, 141-146.
18. A. H. P. de Oliveira, M. L. F. Nascimento and H. P. de Oliveira, Materials Research, 2016, 19, 1080-1087.
19. X. Hong, C. Deng, X. Wang, W. Dong and B. Liang, Journal of Energy Storage, 2022, 53, 105086.
20. S. Li, Q. He, F. Gao, H. Liu, H. Gao, Y. Xue and L. Li, Journal of Alloys and Compounds, 2025, 1010, 177895.
21. P. Patel, A. Pandey, V. Bonu, K. K. Madapu, O. P. Khatri and H. C. Barshilia, Physica B: Condensed Matter, 2025, 705, 417087.
22. X. Liao, Y. Zhao, J. Wang, W. Yang, L. Xu, X. Tian, Y. Shuang, K. A. Owusu, M. Yan and L. Mai, Nano Research, 2018, 11, 2083-2092.
23. M. R. Islam, M. Rahaman, M. M. Billah and M. R. Islam, Materials Advances, 2024, 5, 5307-5321.
24. J. Ran, Y. Liu, T. Yang, H. Feng, H. Zhan and H. Shi, Journal of Energy Storage, 2023, 64, 107216.
25. K. Ashokkumar, S. Dhanapandian, S. Suthakaran and N. Krishnakumar, Materials Today: Proceedings, 2022, 62, 425-428.
26. G. Kresse and J. Furthmüller, Computational materials science, 1996, 6, 15-50.
27. J. P. Perdew, K. Burke and M. Ernzerhof, Physical review letters, 1996, 77, 3865.
28. S. L. Dudarev, G. A. Botton, S. Y. Savrasov, C. Humphreys and A. P. Sutton, Physical Review B, 1998, 57, 1505.
29. D. A. Kitchaev, H. Peng, Y. Liu, J. Sun, J. P. Perdew and G. Ceder, Physical Review B, 2016, 93, 045132.
30. H. V. Thang and G. Pacchioni, The Journal of Physical Chemistry C, 2018, 122, 20880-20887.
31. S. Abbas, T. H. Bokhari, A. Zafar, S. Javed, S. Karim, H. Sun, S. Hussain, A. Khalid, Y. Yu and R. T. A. Khan, Journal of Energy Storage, 2024, 87, 111455.
32. D. A. Tompsett, S. C. Parker and M. S. Islam, Journal of Materials Chemistry A, 2014, 2, 15509-15518.
33. A. Yadav, A. K. Sharma, J. Yadav, S. Bhasker, G. Mishra, H. P. Bhasker, S. P. Patel, P. K. Dhawan and D. K. Chaudhary, Zeitschrift für Naturforschung A, 2025, 80, 345-362.
34. D. İskenderoğlu, K. Ç. Demir, H. Güney and M. E. Güldüren, Advanced Engineering Materials, 2025, e202501856.

35. E. D. Blinov, E. V. Kulchakovskaya, N. A. Sokovikov, V. A. Svetlichnyi, S. A. Kulinich and O. V. Vodyankina, Nanomaterials, 2025, 15, 166.
36. P. Yao, X. Gao, F. Xie, G. Lv, H. Yang, R. Snyders, C. Bittencourt and W. Li, Journal of Alloys and Compounds, 2025, 1014, 178678.
37. I. Elhamdi, H. Souissi, O. Taktak, J. Elghoul, S. Kammoun, E. Dhahri and B. F. Costa, RSC advances, 2022, 12, 13074-13086.
38. M. M. A. Siddiqui, S. Abbas, F. Faiz, A. Zafar, S. Karim, H. Sun, A. Khalid, Y. Faiz, Y. Yu and H. Sultan, New Journal of Chemistry, 2025, 49, 8888-8897.
39. N. Kanaujiya, N. Kumar, A. Srivastava, Y. Sharma and G. D. Varma, Journal of Electroanalytical Chemistry, 2018, 824, 226-237.
40. R. Kumar and R. Thangappan, ENERGY & FUELS, 2024, 38, 11216-11232.
41. M. M. H. Raza, A. S. Alzahrani, M. Al-Rasheidi, M. Y. Bhat and F. Khan, Journal of Alloys and Compounds, 2025, 182265.
42. G. Wang, Y. Wang, B. Guan, J. Liu, Y. Zhang, X. Shi, C. Tang, G. Li, Y. Li and X. Wang, Small, 2021, 17, 2104557.
43. Y. Jiang, D. Ba, Y. Li and J. Liu, Advanced Science, 2020, 7, 1902795.
44. L. Kang, C. Huang, N. Zhang, J. Zhang, C. Luo, C. Wang, X. Zhou and X. Wu, Journal of Alloys and Compounds, 2019, 809, 151790.
45. G. A. Ribeiro, S. L. de Lima, K. E. Santos, J. P. Mendonça, P. Macena, E. C. Pessanha, T. C. Cordeiro, J. Gardener, G. Solórzano and J. E. Fonsaca, Discover Nano, 2023, 18, 147.
46. J. Wu, W. Raza, P. Wang, A. Hussain, Y. Ding, J. Yu, Y. Wu and J. Zhao, Electrochimica Acta, 2022, 418, 140339.
47. Z.-H. Huang, Y. Song, D.-Y. Feng, Z. Sun, X. Sun and X.-X. Liu, ACS nano, 2018, 12, 3557-3567.
48. N. P. Kondekar, M. G. Boebinger, E. V. Woods and M. T. McDowell, ACS applied materials & interfaces, 2017, 9, 32394-32404.
49. H. Dong, C. Gong, R. Addou, S. McDonnell, A. Azcatl, X. Qin, W. Wang, W. Wang, C. L. Hinkle and R. M. Wallace, ACS applied materials & interfaces, 2017, 9, 38977-38983.
50. M. Baker, R. Gilmore, C. Lenardi and W. Gissler, Applied Surface Science, 1999, 150, 255-262.
51. P. Matheswaran, P. Karuppiah and P. Thangavelu, Ionics, 2021, 27, 1769-1780.
52. D. R. Patil, B. Koteswararao, K. Begari, A. Yogi, M. Moussa and D. P. Dubal, ACS Applied Energy Materials, 2019, 2, 2972-2981.
53. Q. Li, J. Zhou, R. Liu and L. Han, Dalton Transactions, 2019, 48, 17163-17168.
54. M. Rittiruam, P. Buapin, T. Saelee, P. Khajondetchairit, S. Kheawhom, B. Alling, S. Praserthdam, A. Ektarawong and P. Praserthdam, Journal of Alloys and Compounds, 2022, 926, 166929.
55. Z. Pan, L. Jin, C. Yang, X. Ji and M. Liu, Chemical Engineering Journal, 2023, 470, 144084.
56. A. Zhang, N. Mao, Y. Zhong, W. Zheng, L. Cui, C. Barrow, J. Razal, W. Yang and J. Liu, Composites Part B: Engineering, 2021, 215, 108756.
57. X. Cheng, L. Zhang, L. Li, H. Wu, J. Zheng, J. Yao and G. Li, Colloids and Surfaces A: Physicochemical and Engineering Aspects, 2025, 709, 136163.
58. Y. Zhang, K. Li, X. Wang, S. Xiong, F. Chen and Y. Li, Scientific Reports, 2026, 16, 301.
59. M. Yu, R. Liu, J. Liu, S. Li and Y. Ma, Small, 2017, 13, 1702616.
60. A. Philip and A. R. Kumar, Journal of Alloys and Compounds, 2025, 1010, 177249.
61. W. Tao, H. Quan, Z. Tu, Z. Zhang and D. Chen, Journal of Colloid and Interface Science, 2025, 683, 1-13.
62. M. Wang, H. Fei, P. Zhang and L. Yin, Electrochimica Acta, 2016, 209, 389-398.
63. D. Sahoo, J. Shakya, S. Choudhury, S. S. Roy, L. Devi, B. Singh, S. Ghosh and B. Kaviraj, ACS omega, 2022, 7, 16895-16905.
64. H. Heydari, M. Abdouss, S. Mazinani, J. S. Shayeh and A. M. Bazargan, Journal of Energy Storage, 2022, 48, 103905.
65. Y. Luo, J. Li, C. Chen and W. Liu, Scientific Reports, 2025, 15, 6393.
66. A. Xu, S. Zhang, L. Yin, W. Cao, Z. Zhao and Y. Qin, Electrochimica Acta, 2025, 524, 146048.
67. M. Abdullah, P. John, K. Jabbour, M. I. Ahmad, S. Khan, M. S. Waheed, M. D. Albaqami, M. Sheikh, M. F. Ehsan and M. N. Ashiq, Journal of Energy Storage, 2024, 78, 110034.

View Article Online
DOI: 10.1039/D5MA01325A

68. H. Quan, W. Zeng, W. Chen, Y. Wang, W. Tao and D. Chen, Journal of Alloys and Compounds, 2023, 938, 168524.
69. S. Ren, S. Zhang, X. Zhang, Y. Jiang, C. Xu, Z. Lei, M. Wei, G. Zhu, Y. Zhao and H. Xu, Journal of Energy Storage, 2025, 128, 117207.
70. X. Zhang, Y. Wei, X. Yang, C. Hou, Y. Chen and D. Wang, Journal of Energy Storage, 2025, 122, 116677.

View Article Online
DOI: 10.1039/D5MA01325A

Data Availability Statement

The authors confirm that the data supporting the findings of this study are available within the article and its supplementary materials.